

Article

Sensitivity Analysis of Entropy Generation in Nanofluid Flow inside a Channel by Response Surface Methodology

Bijan Darbari, Saman Rashidi and Javad Abolfazli Esfahani *

Department of Mechanical Engineering, Ferdowsi University of Mashhad, Mashhad 91775-1111, Iran; Bijan.Darbari@stu.um.ac.ir (B.D.); samanrashidi3983@gmail.com (S.R.)

* Correspondance: abolfazl@um.ac.ir; Tel.: +98-51-3880-5005; Fax: +98-51-3880-7185

Academic Editors: Giulio Lorenzini and Omid Mahian

Received: 20 December 2015; Accepted: 27 January 2016; Published: 5 February 2016

Abstract: Nanofluids can afford excellent thermal performance and have a major role in energy conservation aspect. In this paper, a sensitivity analysis has been performed by using response surface methodology to calculate the effects of nanoparticles on the entropy generation. For this purpose, the laminar forced convection of Al_2O_3 -water nanofluid flow inside a channel is considered. The total entropy generation rates consist of the entropy generation rates due to heat transfer and friction loss are calculated by using velocity and temperature gradients. The continuity, momentum and energy equations have been solved numerically using a finite volume method. The sensitivity of the entropy generation rate to different parameters such as the solid volume fraction, the particle diameter, and the Reynolds number is studied in detail. Series of simulations were performed for a range of solid volume fraction $0 \leq \phi \leq 0.05$, particle diameter $30 \text{ nm} \leq dp \leq 90 \text{ nm}$, and the Reynolds number $200 \leq \text{Re} \leq 800$. The results showed that the total entropy generation is more sensitive to the Reynolds number rather than the nanoparticles diameter or solid volume fraction. Also, the magnitude of total entropy generation, which increases with increase in the Reynolds number, is much higher for the pure fluid rather than the nanofluid.

Keywords: sensitivity analysis; response surface methodology; entropy generation; Al_2O_3 -water nanofluid; finite volume method

1. Introduction

The study of the heat transfer inside a channel has received many attentions due to its numerous applications in energy related engineering problems such as cooling devices in automotive, aerospace industries, heat exchanger systems, heat sinks for electronic components, oil and gas flow in reservoirs, chemical processing, hydrocarbon processing, polymers, pharmaceuticals, food and beverage, chimney stacks, cooling towers, *etc.* The efficiency improvement of this problem is very critical to save the energy and improve the performance. The selection of working fluid is a key issue to improve the thermal performance of flow in a channel. Suspensions of particles with high thermal conductivity in base fluids are one of the innovative techniques to increase the heat transfer rate in channel flows. Many researchers used the conservation laws to simulate the nanofluid flow inside a channel [1,2]. Beside such analysis, an exergy analysis is crucial from the viewpoint of energy management to design an optimum system with low lost work. First, a comprehensive literature review on the papers in this field is necessary to classify these researches.

Some researchers studied the effects of nanoparticles on the heat transfer rate in internal flows [3]. Santra *et al.* [1] investigated the laminar flow of CuO -water nanofluid through two isothermally heated parallel plates. They found that there is a significant growth in heat transfer with increase in solid

volume fraction of nanoparticles for any Reynolds number. Raisi *et al.* [2] performed a numerical study on forced convection laminar nanofluid flow inside a microchannel for both slip and no-slip boundary conditions. They observed that the solid volume fraction of nanoparticles has a negligible influence on the heat transfer rate at low values of the Reynolds number. In another research, Heyhat *et al.* [4] performed an experimental work on the laminar convective heat transfer of nanofluid flow in a horizontal tube. They used Al_2O_3 nanoparticles with water as the base fluid. Their results revealed that the increase in heat transfer coefficient by adding the nanoparticles to the base fluid is about 32% at $\phi = 2\%$ (ϕ is solid volume fraction of nanoparticles). Beside this advantage, they observed an increase in pressure loss for the nanofluid in comparison to the pure water.

Some researchers performed the exergy analysis for nanofluid flow. Mahian *et al.* [5] performed a review of entropy generation in nanofluid flow. They reported that adding nanoparticles to the base fluid could be very fruitful in decreasing the entropy generation. Note that this is depended on the channel size, type of flow regime (*i.e.*, laminar or turbulent) and solid volume fraction of nanoparticles. Malvandi *et al.* [6] investigated analytically the entropy generation of steady nanofluids flow around a flat plate. They used different types of nanoparticles include Cu, Al_2O_3 and TiO_2 . Their results indicated that adding the Cu nanoparticles to the base fluid (water) generates more entropy in comparison to the other nanoparticles. This was due to the high density of Cu particles. Khaleduzzaman *et al.* [7] performed an exergy analysis on water-alumina nanofluid for an electronic liquid cooling system. They found that the friction factor increased with the rise of the solid volume fractions of nanoparticles. In another research, Khairul *et al.* [8] performed an exergy analysis on the metal oxide nanofluid flow in a corrugated plate heat exchanger. They observed an increase in the friction factor, pressure drop and pumping power with increase in particle volume fraction and volume flow rate of nanofluids.

Some researchers performed exergy analysis for flow inside a channel or microchannel [9,10]. Mah *et al.* [11] investigated analytically the effects of viscous dissipation on the entropy generation in laminar fully developed flow of Al_2O_3 -water nanofluid in circular microchannels. They observed that the viscous dissipation has a negligible effect on the entropy generation due to the fluid friction irreversibility. Hajjaligol *et al.* [12] investigated the exergy characteristics of nanofluid flow in a 3-D microchannel under a magnetic field. They found that the contribution of thermal entropy generation in the total is prominent in comparison to the frictional and magnetic one. OzgunKorukcu [13] performed an exergy analysis for the laminar and steady flow across a square obstacle placed in the channel with strong blockage.

Sensitivity analysis applies in engineering problems to determine how different values of an independent variable affect a desired output. This technique is very useful when attempting to determine the impact of several influence parameters on outputs of a problem. Some researchers used this analysis in different thermal engineering problems. Rashidi *et al.* [14] used the sensitivity analysis for porous solar heat exchangers by response surface methodology. In another research, Rashidi *et al.* [15,16] performed the optimization and sensitivity analyses for convective heat transfer of water-alumina nanofluid flow over equilateral triangular cylinder with different orientations. They selected the solid volume fraction of nanoparticles, Reynolds number, and orientation of the obstacle as the input parameters. Also, the drag coefficient and Nusselt number were as output variables. They reported that the Nusselt number and drag coefficient are more sensitive to orientation of the obstacle in comparison to the Reynolds number and solid volume fractions of nanoparticles.

As mentioned earlier, the exergy analysis is necessary for nanofluid flows and can help to engineer when designing the heat transfer equipment. Beside this analysis, it is very important to determine the key parameters in entropy generation for such systems. Such study provides better assessment in design process. The literature review shows that such study is scarce. The main objective of the present study is to determine the sensitivity of the entropy generation to changes of different nanofluid parameters such as solid volume fraction, particle diameter and Reynolds number.

2. Problem Statement and Computational Model

The geometry configuration and coordinate system for this study are presented in Figure 1. In this research, the Al_2O_3 -water nanofluid flow between two parallel plates with half width D and length L with inlet uniform velocity (U_∞) and temperature (T_∞) is considered. The plates are maintained at a constant temperature (T_w).

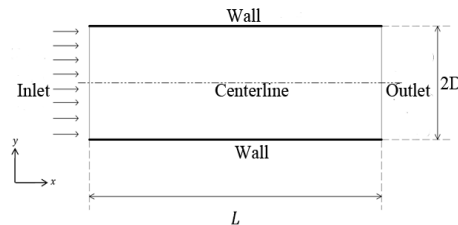


Figure 1. The computational domain and coordinate system.

The following assumptions are made:

- (1) The flow is considered to be two-dimensional, laminar, steady and incompressible.

The simulation results are presented for the range of solid volume fraction $0 \leq \phi \leq 0.05$, particle diameter $30 \text{ nm} \leq dp \leq 90 \text{ nm}$, and Reynolds number $200 \leq \text{Re} \leq 800$. Note that there are many reasons for selecting this range of the Reynolds number in this problem. Some important reasons are listed as follows:

- ✓ This range of Reynolds numbers is significant for designing many devices such as micro devices and compact heat exchangers, which are two important applications of this geometrical (channel).
 - ✓ Higher Reynolds numbers are beyond the limit where two dimensional simulations can be performed [17].
 - ✓ It is safe to drop the viscous dissipation effects in the energy equation at this range of Reynolds number.
- (2) Bottom half of the channel is considered in simulation due to the symmetrical shape.

Governing equations for simulation of this problem are continuity, momentum and energy equations. For a two-dimensional flow, these equations can be written as:

- Conservation of mass equation:

$$\frac{\partial u}{\partial x} + \frac{\partial v}{\partial y} = 0 \quad (1)$$

- Momentum equation in x and y directions [18]:

$$\rho_{eff} \left[u \frac{\partial u}{\partial x} + v \frac{\partial u}{\partial y} \right] = -\frac{\partial p}{\partial x} + \mu_{eff} \left[\frac{\partial^2 u}{\partial x^2} + \frac{\partial^2 u}{\partial y^2} \right] \quad (2)$$

$$\rho_{eff} \left[u \frac{\partial v}{\partial x} + v \frac{\partial v}{\partial y} \right] = -\frac{\partial p}{\partial y} + \mu_{eff} \left[\frac{\partial^2 v}{\partial x^2} + \frac{\partial^2 v}{\partial y^2} \right] \quad (3)$$

- Energy equation [18]:

$$\rho_{eff} C_{eff} \left[u \frac{\partial T}{\partial x} + v \frac{\partial T}{\partial y} \right] = k_{eff} \left[\frac{\partial^2 T}{\partial x^2} + \frac{\partial^2 T}{\partial y^2} \right] \quad (4)$$

where C_{eff} , k_{eff} , ρ_{eff} and μ_{eff} are effective specific heat, conductivity, density and viscosity, respectively.

- The effective density is given by [19]:

$$\rho_{eff} = (1 - \phi)\rho_f + \phi\rho_p \quad (5)$$

where ϕ is the solid volume fraction and subscripts f and p indicate fluid and particle, respectively.

- The effective specific heat is measured by using the following equation [20]:

$$C_{eff} = \frac{(1 - \phi)\rho_f C_f + \phi\rho_p C_p}{\rho_{eff}} \quad (6)$$

- The effective dynamic viscosity is defined in following form [21]:

$$\mu_{eff} = \mu_f + \frac{\rho_p V_B d_p^2}{72N\delta} \quad (7)$$

where N is a non-dimensional function of the nanoparticle diameter, fluid viscosity and solid volume fractions. This function is defined by [21,22]:

$$\begin{aligned} N &= \mu_f^{-1} [(n_1 d_p + n_2) \phi + (n_3 d_p + n_4)] \\ n_1 &= -0.000001113 \frac{\text{kg}}{\text{m}^2 \text{s}}, n_2 = -0.000002771 \frac{\text{kg}}{\text{ms}} \\ n_3 &= 0.00000009 \frac{\text{kg}}{\text{m}^2 \text{s}}, n_4 = -0.000000393 \frac{\text{kg}}{\text{ms}} \end{aligned} \quad (8)$$

where δ and V_B are the distance between nanoparticles and Brownian velocity of the nanoparticles, respectively. These parameters are defined by [21]:

$$V_B = \frac{1}{d_p} \sqrt{\frac{18K_B T}{\pi \rho_p d_p}} \quad (9)$$

$$\delta = \sqrt[3]{\frac{\pi}{6\phi}} d_p \quad (10)$$

where d_p and K_B are nanoparticle diameter (= 30 nm) and Boltzmann constant (= 1.38×10^{-23} J·K⁻¹), respectively.

- Finally, the effective thermal conductivity is calculated by [23]:

$$\frac{k_{eff}}{k_f} = 1 + 64.7 \times \phi^{0.7460} \left(\frac{d_f}{d_p}\right)^{0.3690} \left(\frac{k_p}{k_f}\right)^{0.7476} \times \text{Pr}^{0.9955} \times \text{Re}^{1.2321} \quad (11)$$

where d_f is molecular diameter of the water (= 0.3 nm). The Prandtl and Reynolds numbers in this equation are calculated by:

$$\text{Pr} = \frac{\mu}{\rho_f \alpha_f} \quad (12)$$

$$\text{Re} = \frac{\rho_f K_B T}{3\pi\mu^2 l_{BF}} \quad (13)$$

where l_{BF} is the mean free path of water (= 0.17 nm) and μ is calculated by [18]:

$$\mu = 2.414 \times 10^{-5} \times 10^{\frac{247.8}{T-140}} \quad (14)$$

Generally, the local volumetric entropy generation rate with the convective heat transfer and viscous effects can be calculated by [24]:

$$S_g''' = \frac{k_{eff}}{T^2} \left[\left(\frac{\partial T}{\partial x}\right)^2 + \left(\frac{\partial T}{\partial y}\right)^2 \right] + \frac{\mu_{eff}}{T} \left\{ 2 \left[\left(\frac{\partial u}{\partial x}\right)^2 + \left(\frac{\partial v}{\partial y}\right)^2 \right] + \left[\left(\frac{\partial u}{\partial y}\right) + \left(\frac{\partial v}{\partial x}\right) \right]^2 \right\} \quad (15)$$

The dimensionless local volumetric entropy generation rate is calculated by:

$$N_g = \frac{S_g''' D^2}{k_f} \quad (16)$$

The dimensionless total entropy generation rate per unit depth is obtained by:

$$N_t = \frac{1}{A} \left[\int_{LA} (N_g) dA \right] \quad (17)$$

Following boundary conditions are applied in this problem:

- At the inlet of the channel, a uniform flow is assumed. This boundary is defined by:

$$u = U_\infty, v = 0, T = T_\infty \quad (18)$$

- At the channel wall, no slip and constant temperature boundary conditions are imposed. These boundaries are:

$$u = 0, v = 0, T = T_w \quad (19)$$

- Zero gradient boundary conditions are used at the outlet of the channel [25]. These boundaries are given by:

$$\frac{\partial u}{\partial x} = 0, \frac{\partial v}{\partial x} = 0, \frac{\partial T}{\partial x} = 0 \quad (20)$$

- Symmetry conditions are assumed at the centerline. These boundaries are given by:

$$v = 0, \frac{\partial u}{\partial y} = 0, \frac{\partial T}{\partial y} = 0 \quad (21)$$

To solve numerically the governing equations, pressure base finite volume approach is used. Staggered grid arrangement is applied to store the velocity and pressure components at cell faces and cell center, respectively. The coupling between pressure and velocity is modeled by SIMPLE algorithm [26]. The discretization of the convective and diffusion terms are performed respectively by the third-order accurate QUICK (Quadratic Upstream Interpolation for Convective Kinematics) and Green-Gauss methods.

For all the simulations in this research, it is assumed that the solutions were converged when the summation of residuals were lower than 10^{-7} .

Typical grid used along the computational domain is shown in Figure 2. As shown in this figure, a square two-dimensional mesh is selected for this study. This mesh is refined around the channel wall that the velocity and temperature gradients vary rapidly. The grid independence study is performed with respect to the average Nusselt number at fixed Reynolds number of 200, particle diameter of 30 nm and solid volume fraction of 1%. Four different mesh sizes were generated. The results of grid independence test have been presented in Table 1. As shown in this Table, the difference in the Nusselt number between cases 3 and 4 is 0.3%. Therefore, the grid of case 3 is used for the rest of simulations.

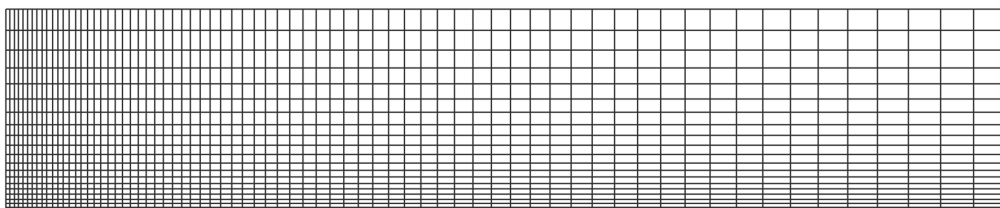
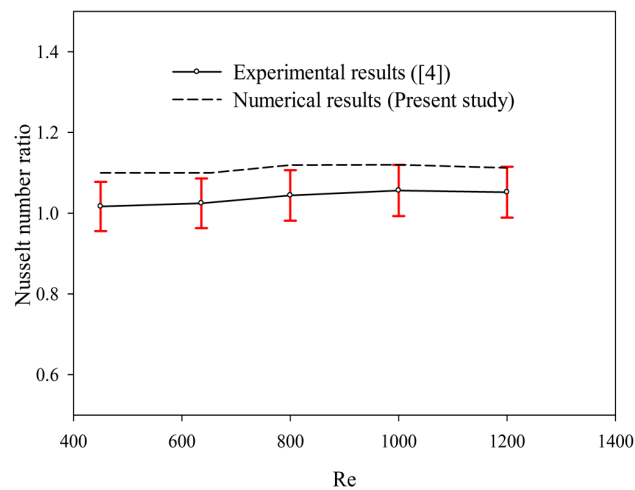


Figure 2. A close view of grid structure for the entrance of the channel.

Table 1. Effect of grid size on Nusselt number at $\phi = 0.01$, $dp = 30$ nm and $Re = 200$.

No.	Grid Size	Nusselt Number	Percentage Difference
1	150 × 20	6.057	1.6
2	300 × 40	6.154	1.1
3	600 × 80	6.222	0.3
4	1200 × 160	6.241	–

The accuracy of the numerical solution is validated by comparison the results with the available experimental data obtained by Heyhat *et al.* [4] as shown in Figure 3. Their experiment was performed for laminar Al_2O_3 -water nanofluid flow inside a horizontal circular duct with a constant surface temperature. Numerical and experimental results are presented for Nusselt number ratio at the solid volume fraction $\phi = 0.01$ and nanoparticle diameter $dp = 40$ nm. The Nusselt number ratio is defined as the ratio of the Nusselt number for the nanofluid to that of pure water. As shown in Figure 3, the numerical results are in agreement with the experimental data. The relative error is about 7%, which is within the error of the experimental data that was reported, as $\pm 6\%$ [4].

**Figure 3.** Comparison between the numerical results and experimental data for the variation of the Nusselt number ratio with Reynolds number.

Response surface methodology is discussed as follows.

Generally, 19 degrees of freedom and 20 runs corresponding to three levels of variables are needed for response surface methodology. Reynolds number (A), particle diameter (B) and solid volume fraction (C) are selected as the input variables in this research. These variables with their levels (*i.e.*, low (−1), central (0) and high (+1) levels) are presented in Table 2.

Table 2. Parameters with their symbol and level.

Parameters	Symbol	Level		
		−1	0	1
Re	A	200	500	800
dp (nm)	B	30	60	90
ϕ	C	0.01	0.03	0.05

Response surface methodology presents some relationships between the several input variables and one or more response variables. The Reynolds number, particle diameter and solid volume fraction are used as input variables and the dimensionless total entropy generation rate is selected as a response

parameter in this study. Box and Wilson [27] first presented this method. They suggested applying a second-degree polynomial model to apply a sequence of designed experiments for obtaining the optimal responses. This model can be summarized in the following mathematical relationship [28]:

$$\text{Res} = \alpha_0 + \alpha_1A + \alpha_2B + \alpha_3C + \alpha_{11}A^2 + \alpha_{22}B^2 + \alpha_{33}C^2 + \alpha_{12}AB + \alpha_{13}AC + \alpha_{23}BC \quad (22)$$

This equation includes 3 linear terms (A, B and C), 3 squared terms (A^2 , B^2 and C^2), 3 two-factor interaction terms (AB, AC and BC) and 1 intercept term. Also, Res is the dimensionless total entropy generation rate and is calculated by coded values [29].

The Central Composite Face centered design (CCF) with $2^a + 2a + b$ experiments is employed to specify the response results. $a = 3$ and $b = 6$ are the number of factors and the number of center points, respectively. As a result, 20 experiments with the Reynolds number (A), the particle diameter (B) and the solid volume fraction (C) as the independent coded variables are needed for this problem. A series of these experiments for nanofluid flow inside the channel are presented at Table 3.

Table 3. Central composite design and response results for nanofluid flow inside the channel.

Standard Order	Coded Value			Real Value			Responses
	A	B	C	Re	dp	ϕ	N_t
1	−1	−1	−1	200	30	0.01	0.014441
2	1	−1	−1	800	30	0.01	0.043037
3	−1	1	−1	200	90	0.01	0.013952
4	1	1	−1	800	90	0.01	0.031240
5	−1	−1	1	200	30	0.05	0.015356
6	1	−1	1	800	30	0.05	0.059118
7	−1	1	1	200	90	0.05	0.014793
8	1	1	1	800	90	0.05	0.038779
9	−1	0	0	200	60	0.03	0.014956
10	1	0	0	800	60	0.03	0.041098
11	0	−1	0	500	30	0.03	0.037220
12	0	1	0	500	90	0.03	0.027376
13	0	0	−1	500	60	0.01	0.026047
14	0	0	1	500	60	0.05	0.033898
15	0	0	0	500	60	0.03	0.031349
16	0	0	0	500	60	0.03	0.031349
17	0	0	0	500	60	0.03	0.031349
18	0	0	0	500	60	0.03	0.031349
19	0	0	0	500	60	0.03	0.031349
20	0	0	0	500	60	0.03	0.031349

Usually, analysis of variance is utilized in response surface methodology (RSM) to benchmark the degree of model accuracy. This analysis is completed by calculating the adjusted mean squares, degree of freedom (DOF), sum of squares, F -value and p -value as the statistical estimators. F -value in this analysis is a measure of variance of data about the mean. The input data shows more accuracy if the F -values to be greater than the unity. Table 4 shows the results of Analysis of Variance (ANOVA) analysis. As shown in this table, the F -values are in the range of $1.74 < F\text{-value} < 1441.41$. This means that the F -value is ample to overcome the requirements. In addition, the model is validated from a statistical point of view by calculating the p -values. It is worth mentioning that the model is validated for the p -values less than 0.05. Table 4 reveals that the model is validated from a statistical point of view, as all p -values are less than 0.05. Note that according to the variance analysis, the regression is significant for the p -values less than 0.01.

Table 4. Analysis of variance.

Source	DOF	Sum of Squares	Contribution	Adj Mean Squares	F-Value	p-Value	–
Model	9	0.002478	99.46%	0.000275	203.17	<0.0001	Significant
Linear	3	0.002249	90.26%	0.000750	553.16	<0.0001	–
A	1	0.001954	78.40%	0.001954	1441.41	<0.0001	–
B	1	0.000185	7.43%	0.000185	136.62	<0.0001	–
C	1	0.000110	4.43%	0.000110	81.45	<0.0001	–
Square	3	0.000039	1.58%	0.000013	9.68	0.0030	–
AA	1	0.000033	1.34%	0.000023	16.72	0.0020	–
BB	1	0.000004	0.14%	0.000005	3.98	0.0074	–
CC	1	0.000002	0.09%	0.000002	1.74	0.0217	–
Interaction	3	0.000190	7.62%	0.000063	46.68	<0.0001	–
AB	1	0.000121	4.85%	0.000121	89.11	<0.0001	–
AC	1	0.000060	2.40%	0.000060	44.09	<0.0001	–
BC	1	0.000009	0.37%	0.000009	6.85	0.0026	–
Residual Error	10	0.000014	0.54%	0.000001	–	–	–
Lack-of-Fit	5	0.000014	0.54%	0.000003	–	–	–
Pure Error	5	0.000000	0.00%	0.000000	–	–	–
Total	19	0.002492	100%	–	–	–	–

Figure 4 presents the residual plots to more benchmark the model accuracy. The normality of the observations is examined by the normal probability plot for residual distribution. The normal probability plot is straight line that this means the regression model is well fitted with the observed values and the model is significant and adequate [29].

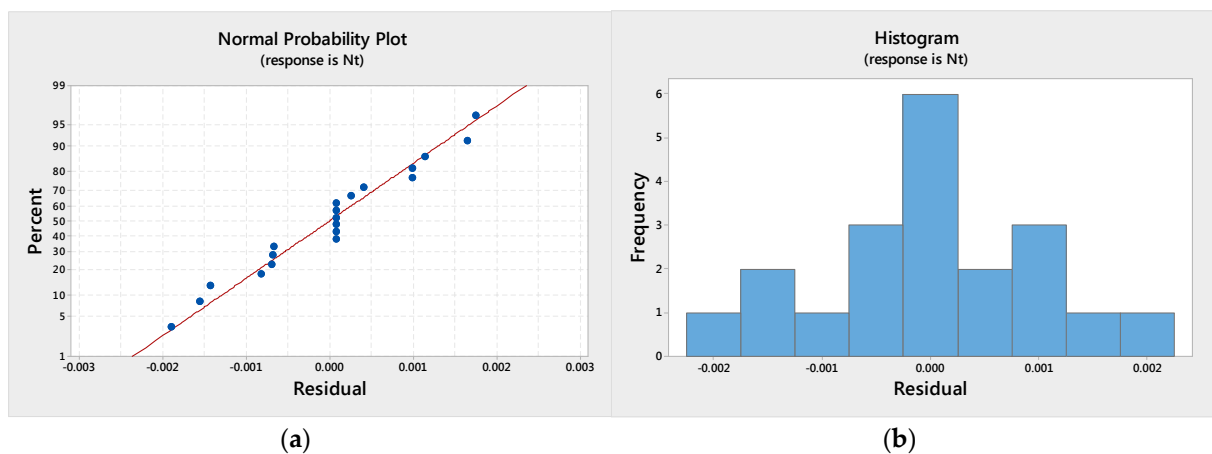


Figure 4. Residual plots (a) Percent; (b) Frequency.

Table 5 presents the regression coefficients of Equation (22) along with the *p*-value of each coefficient. As mentioned earlier, the *p*-values less than 0.05 are acceptable otherwise, they should be removed. Table 5 shows that A, B, C, A², AB, AC and BC are significant terms for the response (*N_t*). As a result, the relationship between response and independent variables can be summarized in following mathematical relationship:

$$N_t = 0.03117 + 0.01398A - 0.00430B + 0.00332C - 0.00287A^2 - 0.00389AB + 0.00273AC - 0.00108BC \tag{23}$$

Finally, the *R*-squared (*R*²) and adjusted *R*-squared (*R*²-adj) are presented in Table 5 to perform more examination of the model accuracy. It can be seen that there is an excellent mathematical

relationship between the independent variables and response as R -squared and adjusted R -squared values are in the vicinity of unity [28].

Table 5. Regression analysis for N_t .

N_t		
Term	Coefficient	p -Value
Constant	0.03117	<0.0001
A	0.01398	<0.0001
B	−0.00430	<0.0001
C	0.00332	<0.0001
A ²	−0.00287	0.0020
B ²	0.00140	0.0740
C ²	−0.00093	0.2170
AB	−0.00389	<0.0001
AC	0.00273	<0.0001
BC	−0.00108	0.0026
–	$R^2 = 99.46\%$	R^2 -adj = 98.97%

Sensitivity analysis is a group of techniques that provides a way to show how a response would be affected by input variables. This analysis can determine the level of response reaction to changes in the values of specific variables. Therefore, it is very important for engineering designs. This analysis provides useful guidelines for engineers during the design process. The sensitivity functions for the response (the total entropy generation rate) are calculated by:

$$\frac{\partial N_t}{\partial A} = 0.01398 - 0.00574A - 0.00389B + 0.00273C \quad (24)$$

$$\frac{\partial N_t}{\partial B} = -0.00430 - 0.00389A - 0.00108C \quad (25)$$

$$\frac{\partial N_t}{\partial C} = 0.00332 + 0.00273A - 0.00108B \quad (26)$$

3. Results and Discussion

The results of CFD and sensitivity analysis are presented in this section. The entropy contours for pure fluid flow at different values of the Reynolds number are charted in Figure 5a. Note that in this figure, solid and dash lines refer to the wall and centerline of the channel, respectively. It can be seen that the total entropy generation increases from near the zero (*i.e.*, 2×10^{-12}) at the centerline to a maximum value (*i.e.*, 7.5×10^{-3}) at the channel wall due to the zero temperature and velocity gradients at the center of the channel, and the comparatively high values of these gradients around the channel wall. It is worth mentioning that the entropy generation has a peak at the entrance of the channel (see red lump) and it decreases along the channel. In addition, the total entropy generation increases with increase in the Reynolds number. Note that the frictional entropy generation becomes more significant for the higher Reynolds numbers. This augmentation in the total entropy generation is in the vicinity of 113% for $200 < Re < 800$. It is worth mentioning that the entropy generation is dominated by the heat transfer irreversibility for low values of the Reynolds numbers.

Figure 5b discloses the effects of solid volume fraction of nanoparticle on the entropy generation contours for nanofluid flow at $Re = 500$ and $dp = 60$ nm. Obviously, the entropy generation increases with increase in the solid volume fraction of nanoparticles. This augmentation in the total entropy generation is in the vicinity of 30% for $0.01 < \phi < 0.05$. This is due to the increase of both the viscosity and thermal conductivity of the nanofluid, which leads to increase in the fluid friction and heat transfer irreversibilities, respectively.

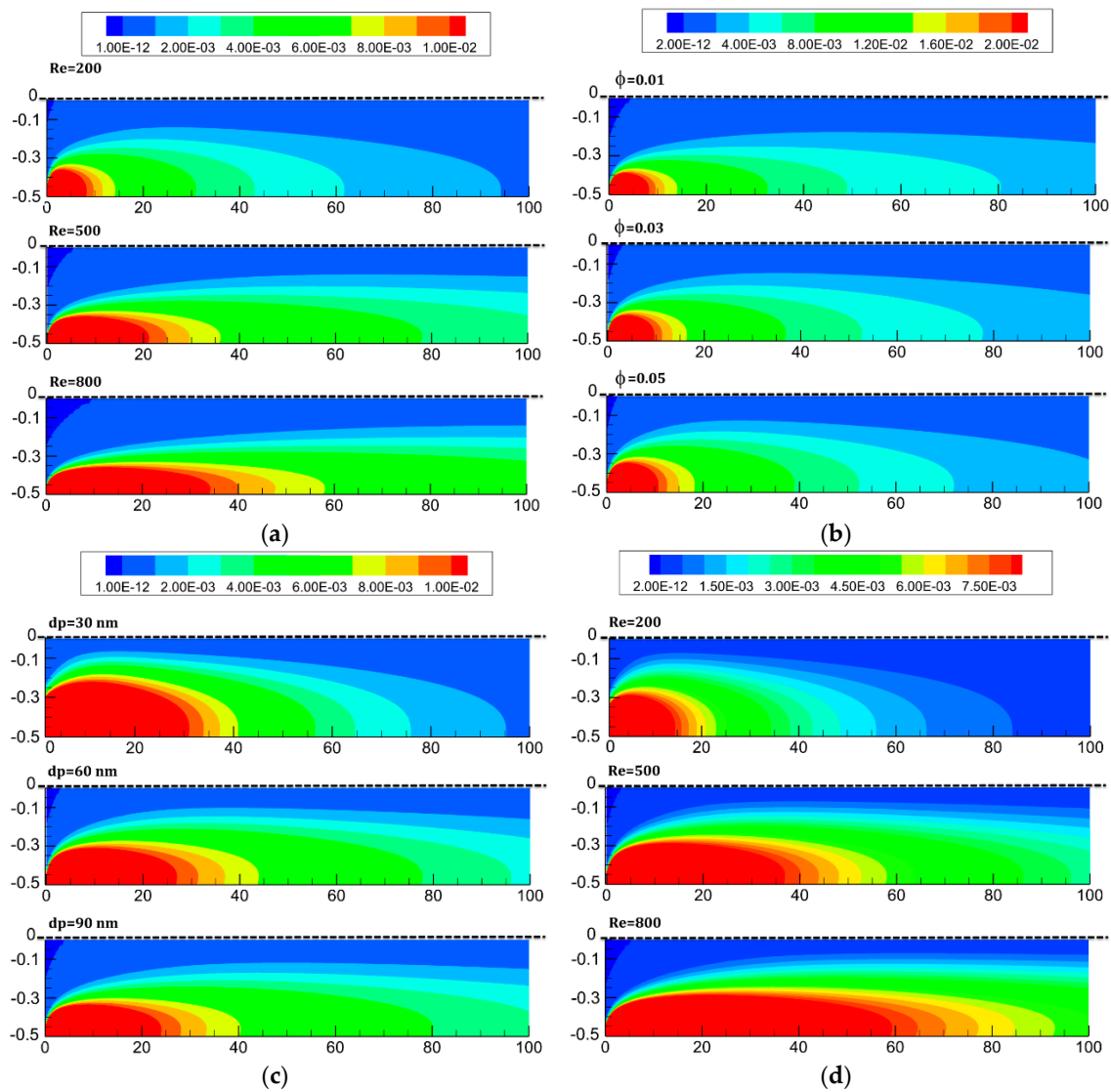


Figure 5. Entropy generation contours for (a) Pure fluid flow at different values of Reynolds number; (b) Nanofluid flow at $Re = 500$, $dp = 60$ nm and different values of solid volume fractions of nanoparticles; (c) Nanofluid flow at $Re = 500$, $\phi = 0.03$ and different values of nanoparticles diameters; (d) Nanofluid flow at $\phi = 0.03$, $dp = 60$ nm and different values of Reynolds numbers.

The effects of nanoparticles diameters on the entropy generation contours for nanofluid flow at $Re = 500$ and $\phi = 0.03$ are examined in Figure 5c. It is indicated that the total entropy generation decreases as nanoparticle diameter increases. This reduction in the total entropy generation is in the vicinity of 32% for $30 < dp < 90$. Note that the thermal entropy generation decreases with increase in the nanoparticle diameter [30]. This is due to the increase in heat transfer rate due to the high thermal conductivity of nanofluids, which is inversely proportional to the nanoparticle diameter at the same solid volume fraction (see Equation (11)). Note that the particles with smaller diameter have higher surface area for interaction with the fluid phase. Also, the frictional entropy generation decreases with increase in nanoparticle diameter. This reduction is due to decrease in the viscosity with increase in the nanoparticle diameter (see Equation (7)). As a result, the frictional and thermal entropy productions follow same trend with increase in the nanoparticle diameter.

Figure 5d shows that how the Reynolds number affect on the total entropy generation contours for nanofluid flow at $\phi = 0.03$ and $dp = 60$ nm. As indicated in this figure, the total entropy generation increases with increase in the Reynolds number. This augmentation in the total entropy generation is

in the vicinity of 175% for $200 < Re < 800$. Comparing to that of pure fluid (Figure 4), the magnitude of total entropy generation, which increases with increase in Reynolds number, is much higher for pure fluid. This indicates that the exergetic effectiveness of Reynolds number in channel flow decreases with the addition of nanoparticle to the base fluid.

Figure 6 shows the Bejan number contour for nanofluid flow at $\phi = 0.05$, $dp = 30$ nm and $Re = 800$. The Bejan number is defined as the ratio of heat transfer irreversibility to total irreversibility (summation of friction and heat transfer irreversibilities). It can be seen that the thermal entropy generation is dominant at all over the domain except in small region at entrance of the channel as the Bejan number is about 0.95. This may be due to the develop of flow along the channel that leads to decrease in friction irreversibility. Note that for fully developed flow $v = 0$, $\frac{\partial v}{\partial y} = 0$, $\frac{\partial v}{\partial x} = 0$ and $\frac{\partial u}{\partial x} = 0$. There are same trends for other values of the Reynolds number, the nanoparticles diameter and the solid volume fraction.

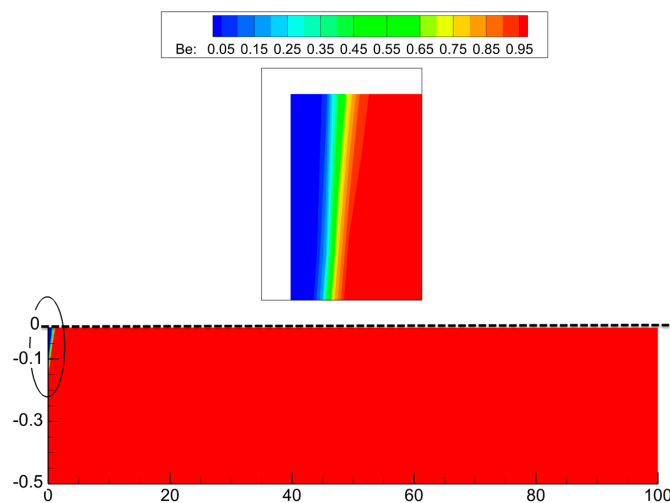


Figure 6. Bejan number contour for nanofluid flow at $\phi = 0.05$, $dp = 30$ nm and $Re = 800$.

The predicted total entropy generation rates as a function of the Reynolds number (A), the nanoparticles diameter (B) and the solid volume fraction of nanoparticle (C) are seen in Figure 7. The effects of the Reynolds number and the nanoparticles diameter on the total entropy generation rate for $C = 0$ ($\phi = 0.03$) are seen in Figure 7a. It is found that the minimum entropy generation occurs near the low level for the Reynolds number. It is worth mentioning that the change in nanoparticles diameter has negligible effect on the entropy generation rate for low values of the Reynolds number. Also, the minimum entropy generation at high values of the Reynolds number occurs near the high level for the nanoparticles diameter. The effects of the Reynolds number and the solid volume fraction on the total entropy generation rate for $B = 0$ ($dp = 60$ nm) are examined in Figure 7b. It can be seen that the minimum entropy generation occurs near the low levels of the Reynolds number and solid volume fraction of nanoparticle. Finally, Figure 7c shows the effects of the nanoparticles diameter and solid volume fraction of nanoparticle on the total entropy generation rate for $A = 0$ ($Re = 500$). It is indicated that the minimum entropy generation occurs near the high level of nanoparticles diameter and the low level of solid volume fraction.

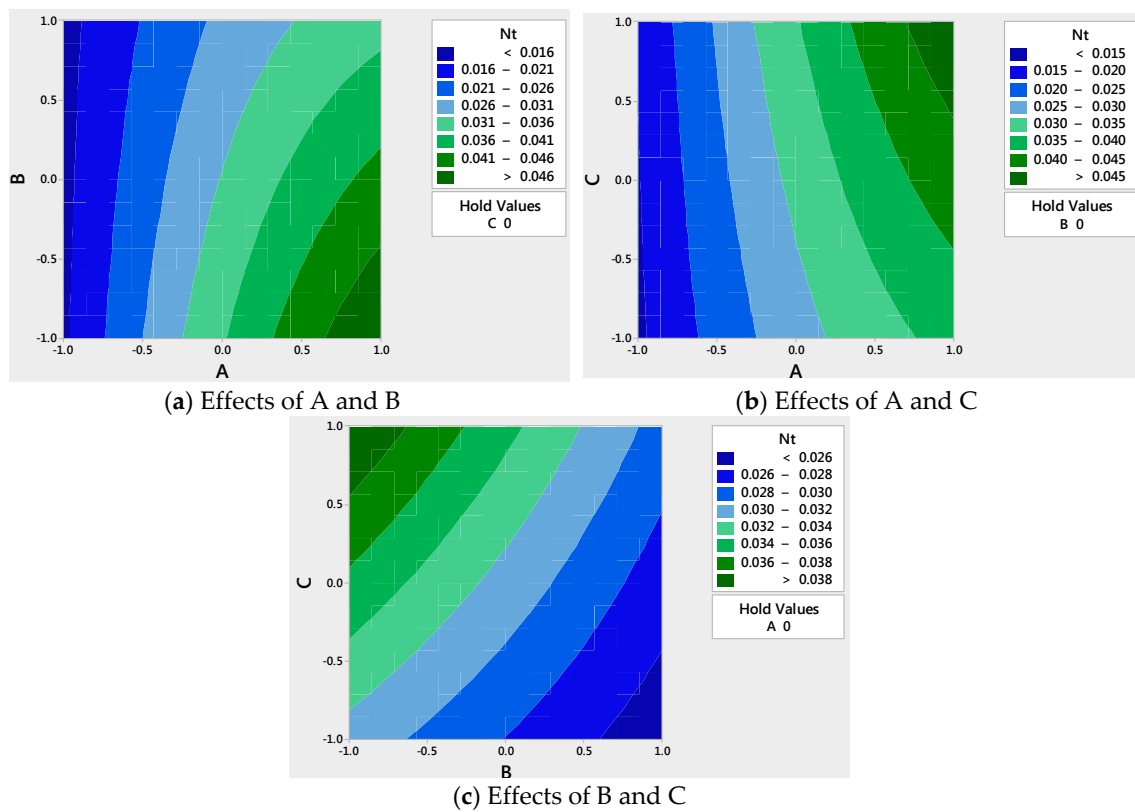


Figure 7. Predicted responses as a function of different factors. (a) Effects of A and B; (b) Effects of A and C; (c) Effects of B and C.

Sensitivity analysis results for different values of the nanoparticles diameter and solid volume fraction are presented in Table 6 and Figure 8. Note that these are determined by utilizing Equations (24)–(26). It is worth mentioning that the response increases with increase in the design parameters for positive values of sensitivity conversely, the negative values of sensitivity reveal that an increase in input variables leads to decrease in the response. The sensitivities of the total entropy generation rate to different parameters at $Re = 500$ ($A = 0$), different values of nanoparticles diameter $dp = 30, 60,$ and 90 nm ($B = -1, 0$ and 1) and the solid volume fraction $\phi = 0.01, 0.03$ and 0.05 ($C = -1, 0$ and 1) are presented in Figure 8. As shown in this figure, the total entropy generation is more sensitive to the Reynolds number rather than the nanoparticles diameter or solid volume fraction. The sensitivities of the total entropy generation to the Reynolds number and nanoparticles diameter increase with increase in the solid volume fraction. Also, the sensitivity of the total entropy generation to the solid volume fraction is constant at different values of it. Moreover, by comparing the results shown in Figure 8a–c, we can conclude that the sensitivities of total entropy generation to the Reynolds number and the solid volume fraction decrease with increase in nanoparticles diameter.

Table 6. Sensitivity analysis of responses, $A = 0$.

B	C	Sensitivity		
		$\frac{\partial Nt}{\partial A}$	$\frac{\partial Nt}{\partial B}$	$\frac{\partial Nt}{\partial C}$
-1	-1	0.0151	-0.0032	0.0044
	0	0.0179	-0.0043	0.0044
	1	0.0206	-0.0054	0.0044
0	-1	0.0113	-0.0032	0.0033
	0	0.0140	-0.0043	0.0033
	1	0.0167	-0.0054	0.0033

Table 6. Cont.

B	C	Sensitivity		
		$\frac{\partial Nt}{\partial A}$	$\frac{\partial Nt}{\partial B}$	$\frac{\partial Nt}{\partial C}$
1	-1	0.0074	-0.0032	0.0022
	0	0.0101	-0.0043	0.0022
	1	0.0128	-0.0054	0.0022

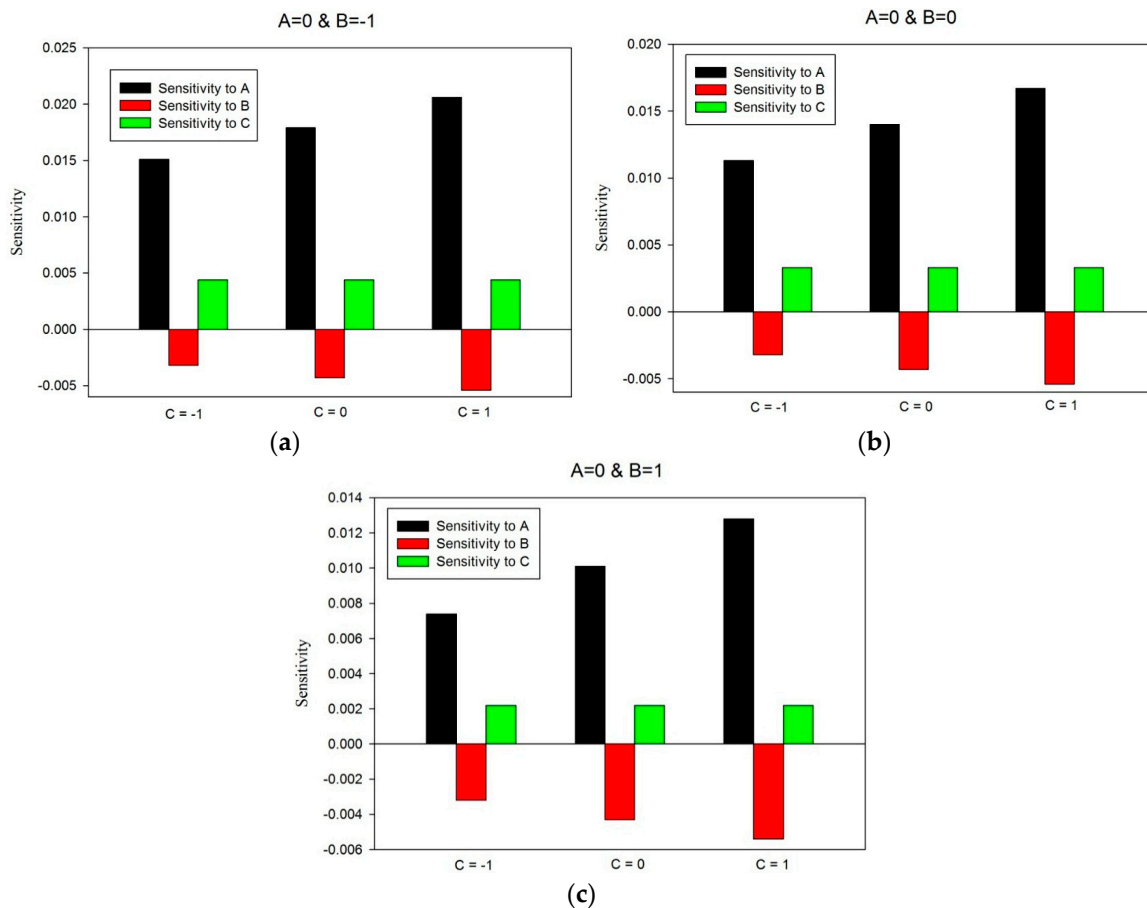


Figure 8. Sensitivity analysis results (a) A = 0 and B = -1; (b) A = 0 and B = 0; (c) A = 0 and B = 1.

4. Conclusions

Laminar nanofluid flow and convective heat transfer in a channel were investigated numerically. The numerical solution method was validated by comparing the simulated results with experimental data for internal flow. An exergy analysis was performed by using velocity and temperature gradients. Beside this, a sensitivity analysis was arranged by response surface methodology to specify the sensitivity of the total entropy generation to different parameters such as the Reynolds number, nanoparticles diameter and solid volume fraction. The main findings of this research are summarized as follows:

- The total entropy generation for nanofluid increases with increase in the Reynolds number and solid volume fraction. These augmentations are in the vicinity of 175% and 30% for $200 < Re < 800$ and $0.01 < \phi < 0.05$, respectively.
- The total entropy generation decreases with increase in the nanoparticles diameter. This reduction is in the vicinity of 32% for $30 < dp < 90$.
- The magnitude of total entropy generation, which increases with increase in the Reynolds number, is much higher for pure fluid rather than the nanofluid.

- The change in nanoparticles diameter has negligible effect on the entropy generation rate for low values of the Reynolds number.
- The total entropy generation is more sensitive to the Reynolds number rather than the nanoparticles diameter or solid volume fraction.
- The sensitivities of the total entropy generation to the Reynolds number and nanoparticles diameter increase with increase in the solid volume fraction.
- The sensitivities of the total entropy generation to the Reynolds number and the solid volume fraction decrease with increase in nanoparticles diameter.

Author Contributions: This paper was prepared using the contributions of all the authors. All authors have read and approved the final manuscript.

Conflicts of Interest: The authors declare no conflict of interest.

Nomenclature

a	number of factors (-)
ANOVA	analysis of variance (-)
K_b	Boltzmann constant (-)
Be	Bejan number (-)
b	number of center points (-)
C	specific heat at constant pressure ($J \cdot kg^{-1} \cdot K^{-1}$)
CCD	central composite design (-)
CCF	central composite face centered (-)
D	half of the channel gap (m)
d_f	molecular diameter of base fluid (nm)
dp	nanoparticle diameter (nm)
DOE	design of experiments (-)
h	heat transfer coefficient ($W \cdot m^{-2} \cdot K^{-1}$)
k	thermal conductivity ($W \cdot m^{-1} \cdot K^{-1}$)
L	length of the channel (m)
l_{BF}	mean free path of water (-)
N_g	dimensionless local volumetric entropy generation rate (-)
N_t	dimensionless total entropy generation rate (-)
p	pressure (Pa)
Pe	Peclet number ($Re \times Pr$)
Pr	Prandtl number (ν/α)
Re	Reynolds number ($\rho U_\infty D \mu^{-1}$)
Res	response (-)
RSM	response surface methodology (-)
S_g'''	entropy generation rate ($W \cdot m^{-3} \cdot K^{-1}$)
T	temperature (K)
u, v	velocity component in x and y directions, respectively ($m \cdot s^{-1}$)
x, y	rectangular coordinates components (m)

Greek Symbols

α	thermal diffusivity of fluid ($m^2 \cdot s^{-1}$)
μ	dynamic viscosity ($kg \cdot m^{-1} \cdot s^{-1}$)
ν	kinematic viscosity ($m^2 \cdot s^{-1}$)

ρ	density of the fluid ($\text{kg} \cdot \text{m}^{-3}$)
ϕ	solid volume fraction (-)
δ	distance between particles (nm)
∞	free stream (-)

Subscripts/Superscripts

B	Brownian (-)
<i>eff</i>	effective
f	fluid
P	particle-pressure (-)
s	solid
w	wall

References

- Santra, A.K.; Sen, S.; Chakraborty, N. Study of heat transfer due to laminar flow of copper–water nanofluid through two isothermally heated parallel plates. *Int. J. Therm. Sci.* **2009**, *48*, 391–400. [[CrossRef](#)]
- Radisi, A.; Ghasemi, B.; Aminossadati, S.M. A numerical study on the forced convection of laminar nanofluid in a microchannel with both slip and no-slip conditions. *Numer. Heat Transf.* **2011**, *59*, 114–129.
- Bianco, V.; Manca, O.; Nardini, S. Performance analysis of turbulent convection heat transfer of Al_2O_3 water-nanofluid in circular tubes at constant wall temperature. *Energy* **2014**, *77*, 403–413. [[CrossRef](#)]
- Heyhat, M.M.; Kowsary, F.; Rashidi, A.M.; Momenpour, M.H.; Amrollahi, A. Experimental investigation of laminar convective heat transfer and pressure drop of water-based Al_2O_3 nanofluids in fully developed flow regime. *Exp. Therm. Fluid Sci.* **2013**, *44*, 483–489. [[CrossRef](#)]
- Mahian, O.; Kianifar, A.; Kleinstreuer, C.; Al-Nimr, M.A.; Pop, I.; Wongwises, S.; Sahin, A.Z. A review of entropy generation in nanofluid flow. *Int. J. Heat Mass Transf.* **2013**, *65*, 514–532. [[CrossRef](#)]
- Malvandi, A.; Ganji, D.D.; Hedayati, F.; Rad, E.Y. An analytical study on entropy generation of nanofluids over a flat plate. *Alex. Eng. J.* **2013**, *52*, 595–604. [[CrossRef](#)]
- Khaleduzzaman, S.S.; Sohel, M.R.; Saidur, R.; Mahbubu, I.M.; Shahrul, I.M.; Akash, B.A.; Selvaraj, J. Energy and exergy analysis of alumina–water nanofluid for an electronic liquid cooling system. *Int. Commun. Heat Mass Transf.* **2014**, *57*, 118–127. [[CrossRef](#)]
- Khairul, M.A.; Mahbubul, I.M.; Saidur, R.; Hepbasli, A.; Hossain, A. Heat transfer performance and exergy analyses of a corrugated plate heat exchanger using metal oxide nanofluids. *Int. Commun. Heat Mass Transf.* **2014**, *50*, 8–14. [[CrossRef](#)]
- Mahmud, S.; Fraser, R.A. Thermodynamic analysis of flow and heat transfer inside channel with two parallel plates. *Int. J. Heat Mass Transf.* **2002**, *2*, 140–146. [[CrossRef](#)]
- Bianco, V.; Manca, O.; Nardini, S. Second law analysis of Al_2O_3 -Water nanofluid turbulent forced convection in a circular cross section tube with constant wall temperature. *Adv. Mech. Eng.* **2013**, *5*, 920278. [[CrossRef](#)]
- Mah, W.H.; Hung, Y.M.; Guo, N. Entropy generation of viscous dissipative nanofluid flow in microchannels. *Int. J. Heat Mass Transf.* **2012**, *55*, 4169–4182. [[CrossRef](#)]
- Hajjaligol, W.; Fattahi, A.; Haji-Ahmadi, M.; EbrahimQomi, M.; Kakoli, E. MHD mixed convection and entropy generation in a 3-D microchannel using Al_2O_3 -water nanofluid. *J. Taiwan Inst. Chem. Eng.* **2015**, *46*, 30–42. [[CrossRef](#)]
- Korukcu, M.O. 2D temperature analysis of energy and exergy characteristics of laminar steady flow across a square cylinder under strong blockage. *Entropy* **2015**, *17*, 3124–3151. [[CrossRef](#)]
- Rashidi, S.; Bovand, M.; Esfahani, J.A. Heat transfer enhancement and pressure drop penalty in porous solar heat exchangers: A sensitivity analysis. *Energy Convers. Manag.* **2015**, *103*, 726–738. [[CrossRef](#)]
- Rashidi, S.; Bovand, M.; Esfahani, J.A. Structural optimization of nanofluid flow around an equilateral triangular obstacle. *Energy* **2015**, *88*, 385–398. [[CrossRef](#)]
- Rashidi, S.; Bovand, M.; Esfahani, J.A.; Ahmadi, G. Discrete particle model for convective Al_2O_3 -water nanofluid around a triangular obstacle. *Appl. Therm. Eng.* **2016**. in press.

17. Breuer, M.; Bernsdorf, J.; Zeiser, T.; Durst, F. Accurate computations of the laminar flow past a square cylinder based on two different methods: Lattice-Boltzmann and finite-volume. *Int. J. Heat Fluid Flow* **2000**, *21*, 186–196. [[CrossRef](#)]
18. Valipour, M.S.; Masoodi, R.; Rashidi, S.; Bovand, M.; Mirhosseini, M. A numerical study of convection around a square porous cylinder using Al₂O₃-H₂O Nanofluid. *Therm. Sci.* **2014**, *18*, 1305–1314. [[CrossRef](#)]
19. Bovand, M.; Rashidi, S.; Esfahani, J.A. Enhancement of heat transfer by nanofluids and orientations of the equilateral triangular obstacle. *Energy Convers. Manag.* **2015**, *97*, 212–223. [[CrossRef](#)]
20. Zhou, S.Q.; Ni, R. Measurement of the specific heat capacity of water-based Al₂O₃ nanofluid. *Appl. Phys. Lett.* **2008**, *92*, 093–123. [[CrossRef](#)]
21. Masoumi, N.; Sohrabi, N.; Behzadmehr, A. A new model for calculating the effective viscosity of nanofluids. *J. Appl. Phys. D* **2009**, *42*, 055501. [[CrossRef](#)]
22. Rashidi, S.; Bovand, M.; Esfahani, J.A. Opposition of Magnetohydrodynamic and Al₂O₃-water nanofluid flow around a vertex facing triangular obstacle. *J. Mol. Liq.* **2016**, *215*, 276–284. [[CrossRef](#)]
23. Chon, C.H.; Kihm, K.D.; Lee, S.P.; Choi, S.U. Empirical correlation finding the role of temperature and particle size for nanofluid (Al₂O₃) thermal conductivity enhancement. *Appl. Phys. Lett.* **2005**, *87*, 153107. [[CrossRef](#)]
24. Bejan, A. A study of entropy generation in fundamental convective heat transfer. *J. Heat Transf.* **1979**, *101*, 718–729. [[CrossRef](#)]
25. Esfahani, J.A.; Shahabi, P.B. Effect of non-uniform heating on entropy generation for the laminar developing pipe flow of a high Prandtl number fluid. *Energy Convers. Manag.* **2010**, *51*, 2087–2097. [[CrossRef](#)]
26. Patankar, S. *Numerical Heat Transfer and Fluid Flow*; CRC Press: Boca Raton, FL, USA, 1980.
27. Box, G.E.P.; Wilson, K.B. On the experimental attainment of optimum conditions. *J. R. Stat. Soc. Ser. B* **1951**, *13*, 1–45.
28. Montgomery, D.C. *Design and Analysis of Experiments*; Wiley: Hoboken, NJ, USA, 1996.
29. Bovand, M.; Valipour, M.S.; Dincer, K.; Eiamsa-ard, S. Application of Response Surface Methodology to optimization of a standard Ranque–Hilsch vortex tube refrigerator. *Appl. Therm. Eng.* **2014**, *67*, 545–553. [[CrossRef](#)]
30. Yarmand, H.; Ahmadi, G.; Gharekhani, S.; Kazi, S.N.; Safaei, M.R.; Sadat-Alehashem, M.; Mahat, A.B. Entropy generation during turbulent flow of zirconia-water and other nanofluids in a square cross section tube with a constant heat flux. *Entropy* **2014**, *16*, 6116–6132. [[CrossRef](#)]



© 2016 by the authors; licensee MDPI, Basel, Switzerland. This article is an open access article distributed under the terms and conditions of the Creative Commons by Attribution (CC-BY) license (<http://creativecommons.org/licenses/by/4.0/>).